Generalized Analog Least Mean Square Loop for Self-Interference Cancellation in In-Band Full-Duplex Communications

Keda Xu, Anh Tuyen Le, *Member*, *IEEE*, Xiaojing Huang, *Senior Member*, *IEEE*, and Heung-Gyoon Ryu, *Member*, *IEEE*

***Abstract*—This paper introduces a novel method for radio frequency (RF) self-interference (SI) cancellation in in-band full-duplex (IBFD) communication systems using a generalized analog least mean square (GALMS) loop. Conventional research in this area has predominantly focused on employing the tapped delay line (DL) structure to process the RF transmitted signal. The proposed GALMS loop utilizes a filter bank applied on the baseband transmitted signal to avoid the limitation of the conventional tapped DL adaptive filters, which require tapped spacing to satisfy the Nyquist principle. We utilize frequency domain representation and steady-state analysis to derive the modeling error and residual SI power of the proposed structure. Notably, the GALMS loop incorporating an allpass filter bank can achieve the same level of SI cancellation as the conventional DL structure with a significantly reduced number of taps. Simulations are conducted to validate the efficiency of the proposed GALMS loop and prove the theoretical findings.**

***Index Terms*—GALMS loop, self-interference cancellation, filter bank, modeling error, residual signal power.**

I. Introduction

Wireless communication technologies have undergone significant research and development to address the escalating demand for mobile data traffic while alleviating spectrum resource constraints [1]–[3]. Amid such efforts, in-band full-duplex (IBFD) technology, which allows simultaneous transmission and reception on the same frequency band, emerges as a promise for the next-generation wireless networks [4], [5]. However, IBFD transceivers face a significant obstacle — self-interference (SI) [6], a replica of the transmitted signal leaking into the receiver, complicating the distinction between desired and unwanted signals. The magnitude of the SI is substantial, potentially eclipsing the intended received signal and compromising communication quality. To address this challenge, a multifaceted approach is required [7], [8]. Current methods for mitigating SI can be categorized into three primary types: propagation domain cancellation, digital domain cancellation, and analog domain cancellation. Each category possesses its own distinct characteristics [9].

Keda Xu (Corresponding author), Anh Tuyen Le, and Xiaojing Huang are with the Faculty of Engineering and IT, University of Technology Sydney, Ultimo, NSW 2007, Australia (e-mail: keda.xu@student.uts.edu.au; anhtuyen.le@uts.edu.au and xiaojing.huang@uts.edu.au).

Heung-Gyoon Ryu is with the College of Electrical and Computer Engineering, Chungbuk National University, Cheongju 28644, South Korea (e-mail: ecomm@cbu.ac.kr).

Propagation domain cancellation is directly incorporated into the transmission process by adjusting the angle and distance between transmitting and receiving antennas to reduce SI power arriving at the receiver [10], [11]. This technique is usually constrained by spatial availability in the radio front-end [12]. Additionally, this method often struggles with achieving sufficient cancellation across a broad range of frequencies, leading to performance degradation in environments with high multipath effects. The reliance on precise alignment and calibration of the antennas also introduces complexity in implementation and maintenance, potentially increasing the overall cost and reducing the robustness of the system in dynamic or mobile applications. Furthermore, antenna-based SI cancellation can be less effective in mitigating non-linear distortions, necessitating supplementary cancellation techniques to achieve satisfactory performance [13]–[15].

In the digital domain, the SI channel is estimated and then used to convolve with the digital baseband symbols to generate a cancellation signal [16], [17]. Digital SI cancellation techniques, while effective, face several challenges that can limit their practicality. The computational complexity involved in modeling and subtracting the SI signal requires significant processing power, particularly when dealing with wideband signals, which can lead to increased power consumption and potential system delays. This delay can be problematic in real-time communication systems where low latency is essential [18]. Furthermore, digital SI cancellation requires precise synchronization between the transmitted and received signals to ensure accurate cancellation, which can be difficult to achieve, especially in dynamic environments [19], [20].

Analog domain cancellation is crucial in managing high-power SI and protecting the analog-to-digital converter (ADC) from saturation. By mitigating the SI signal in the analog domain before digital conversion, this method prevents the signal from surpassing the dynamic range of the ADC, preserving the integrity of the signal and enhancing overall system reliability [21], [22]. Additionally, analog domain SI cancellation offers the advantage of reducing the computational burden on digital processing, as significant interference is removed before reaching the digital domain. This approach not only improves power efficiency but also allows for the effective handling of wideband signals and complex interference patterns, making it effective in scenarios where other methods might struggle. Hence, analog domain SI cancellation has distinguished itself

among numerous methods [23]–[25].

The core idea of analog domain cancellation lies in generating a radio frequency (RF) signal to cancel SI at the receiver's input. Two primary methods are employed to mitigate SI: passive and active [26]. The passive method generates a cancellation signal using passive components such as transformers or couplers. While effective at canceling the direct path of SI, this method cannot cancel the SI caused by reflections from surrounding obstacles [27]. On the other hand, the active method relies on adjustable weighting coefficients to modify both the amplitude and phase of reference signals derived from the RF transmitted signal. By adapting these coefficients, active analog SI cancellation can efficiently cancel SI across both direct and reflective paths [28]. For instance, the multi-tap analog canceller in [29], leveraging 64 ideal taps, demonstrated an average cancellation exceeding 45 dB across a 200 MHz bandwidth with realistic system configurations.

Many adaptive analog SI cancellation circuits are based on the tapped delay line (DL) structure [30]–[33]. It consists of a series of tapped delay elements that introduce time delays to the transmitted signal, creating a set of shifted versions, which will be used as reference signals for the adaptive filter. Each tap is associated with an adjustable weighting coefficient, and the filter output is the weighted sum of these delayed signals. The least mean square algorithm is commonly used to adjust the weights to minimize the mean square error between the filter's output and a desired signal [34]. It has been shown in [23] and [31] that the delay difference between two consecutive taps is normally required to be shorter than the symbol duration. Additionally, the longest delay time in the filter needs to cover the whole delay spread in the SI channel to achieve an adequate cancellation level. These requirements follow the Nyquist principle so that the adaptive filter can reconstruct the SI channel successfully.

However, tapped DL adaptive filters face a significant challenge when applied to high-speed IBFD wireless systems, such as millimeter wave (mm-wave) and terahertz systems. In such high-speed systems, the transmitted symbol duration is very narrow so that the tap delay becomes exclusively short, and a large number of taps in the filter is required [30], [35]. This leads to increased complexity in circuit design, as the system must accommodate a large number of components to achieve the desired signal replication. Additionally, due to the small wavelength of the transmitted signal, which is very sensitive to the length of the microstrip trace, achieving the desired delay time in mm-wave frequency is challenging [36], [37]. Therefore, implementing the tapped DL structure with a large number of taps in mm-wave IBFD systems may not be practical.

This paper proposes a novel multi-tap adaptive filter structure named the generalized analog least mean square (GALMS) loop. The proposed structure goes beyond the conventional tapped DL framework by incorporating a filter bank at the baseband instead of the RF frontend to generate reference signals. By adopting this generalized structure, we can relax the requirement that tapped spacing must satisfy the Nyquist sampling principle. Notably, our GALMS loop maintains robust performance even in under-sampling scenarios. This advancement results in a remarkable reduction in the number of taps, consequently simplifying circuit design. Furthermore, generating reference signals in the baseband is very useful in avoiding the sensitivity of mm-wave RF signals to microstrip trace in conventional DL adaptive filters. Note that generating reference signals in baseband may not be able to capture the nonlinearities of the SI. However, it is possible to adopt the nonlinear parameter estimation techniques proposed in [38] to generate the nonlinear cancellation signal in baseband and up-convert it to RF by an additional digital-to-analog converter (DAC) as the reference signal for the GALMS loop, which will be our future work.

The contributions of this paper are four-fold:

- Development of the GALMS Loop: We introduce a novel GALMS loop tailored specifically for analog SI cancellation in IBFD communication systems. This new approach addresses the limitations of conventional tapped DL adaptive filters, offering enhanced SI cancellation capabilities.
- Filter Bank Implementation: The GALMS loop utilizes a filter bank that processes the baseband transmitted signal. This approach significantly reduces the required number of taps compared to traditional DL adaptive filters, leading to a more efficient SI cancellation process while maintaining high performance.
- Quantitative Analysis of Performance: We derive the modeling error and residual SI power associated with the proposed GALMS structure using frequency domain representation and steady-state analysis. This detailed quantitative analysis provides a deep understanding of the performance benefits of the GALMS loop.
- Theoretical and Simulation Validation: Theoretical insights gained from our analysis are validated through comprehensive simulations. These simulations demonstrate that the GALMS loop outperforms conventional methods in terms of SI cancellation effectiveness, offering a substantial reduction in system complexity for IBFD systems.

The subsequent sections of this paper are structured as follows. In Section II, the GALMS loop is proposed, which is primarily divided into two parts: generalized filter bank and overall structural analysis. In Section III, we assume a single-carrier system for modeling the interference channel and perform the theoretical derivations for the SI modeling and the residual interference power. In Section IV, simulations are carried out to validate the feasibility of the proposed GALMS loop. Finally, Section V concludes the paper.

II. GALMS ARCHITECTURE AND SIGNAL MODELS

A. Generalized Filter Bank Structure

Denoting the baseband transmitted signal as $X(t)$, its up-converted RF signal can be expressed as $x(t) = \mathrm{Re}\{X(t)e^{j2\pi f_c t}\}$, where f_c represents the carrier frequency. In a single carrier system, $X(t)$ can be represented as

$$X(t) = \sum_{i=-\infty}^{\infty} a_i p(t - iT_s) \tag{1}$$

where a_i represents the complex data symbol, with symbol interval T_s and pulse shaping filter $p(t)$. These complex data

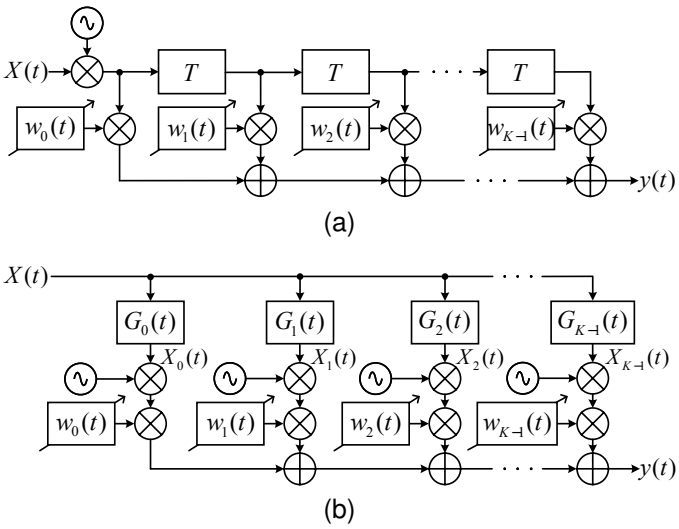

Fig. 1. (a) Conventional multi-tap adaptive filter with tapped DL, (b) The proposed generalized adaptive filter structure.

symbols are assumed to be independent and meet the condition $E\{a_i^* a_{i'}\} = \begin{cases} 1, & i = i' \\ 0, & i \neq i' \end{cases}$, where a_i^* is the conjugate of a_i and $E\{\cdot\}$ is the ensemble expectation. The average power of $X(t)$ is $V_X^2 = \frac{1}{T_s}\int_0^{T_s} E\{|X(t)|^2\}dt$ over 1 Ω load.

The analog adaptive filter that generates the SI cancellation signal is designed with K taps. Each tap is endowed with weighting coefficients $w_k(t)$, $k = 0, 1, \cdots, K-1$. $G_k(t)$ represents the k-th baseband filter, and $X_k(t) = G_k(t) * X(t)$ is the baseband transmitted signal passing through the k-th filter where $*$ is the linear convolution operation.

Fig. 1 presents a conventional multi-tap adaptive filter structure equipped with the tapped DL and the proposed generalized counterpart with the filter bank. It can be observed that the tapped DL structure in Fig. 1(a) typically adopts a cascaded accumulation model where each delay element introduces a delay T. In contrast, the generalized filter bank in Fig. 1(b) employs parallel transmission paths, each with the baseband filter $G_k(t)$. Additionally, compared to the analog signal processing at the RF frontend discussed in [23], the generalized filter bank operates at baseband, leading to simpler circuits and low-cost implementation.

In fact, according to the property of the Dirac delta function $X(t - kT) = \delta(t - kT) * X(t)$, the tapped DL depicted in Fig. 1(a) is also a special case of the generalized structure represented by Fig. 1(b). Therefore, we can express the RF cancellation signal $y(t)$ in both structures as

$$y(t) = Re\Big\{ \sum_{k=0}^{K-1} w_k^*(t)[G_k(t) * X(t)]e^{j2\pi f_c t} \Big\}. \tag{2}$$

B. GALMS Loop

Fig. 2 illustrates the proposed GALMS loop for SI cancellation in IBFD systems, where the bold line in the diagram represents the passage of the complex I/Q signal. The proposed GALMS loop utilizes a filter bank to generate reference signals in the baseband shown in Fig. 1(b) and an analog

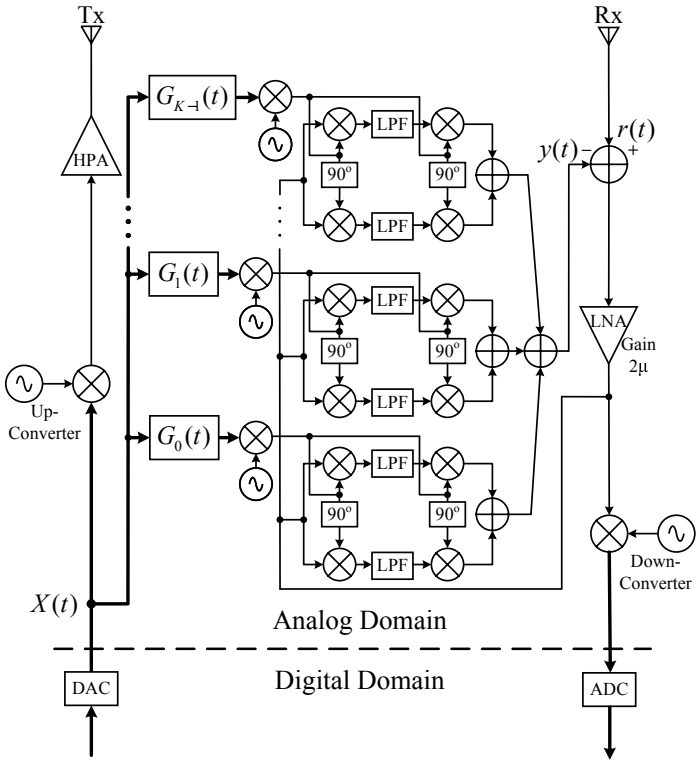

Fig. 2. The proposed generalized analog least mean square loop.

least mean square (ALMS) loop circuitry to update weighting coefficients without requiring digital signal processing. The adaptive filter aims to minimize the power of the residual signal $d(t) = r(t) - y(t)$, where $r(t)$ is the received RF signal. According to the least mean square principle, the convergence of each weighting coefficient $w_k(t)$ is governed by the integration over $\partial d^2(t)/\partial w_k(t)$, where

$$\begin{aligned} \frac{\partial d^2(t)}{\partial w_k(t)} &= \frac{\partial [r(t) - y(t)]^2}{\partial Re\{w_k(t)\}} + j\frac{\partial [r(t) - y(t)]^2}{\partial Im\{w_k(t)\}} \\ &= -2[r(t) - y(t)][G_k(t) * X(t)]e^{j2\pi f_c t}. \end{aligned} \tag{3}$$

Given the challenges associated with implementing an ideal RF integration circuit, a more practical alternative is proposed using an ALMS circuit described by a differential equation [23]

$$\frac{dw_k(t)}{dt} + \alpha w_k(t) = -\frac{\mu\alpha}{K_1 K_2}\frac{\partial d^2(t)}{\partial w_k(t)}, k = 0, 1, \cdots, K-1 \tag{4}$$

where α, μ, K_1 and K_2 are constants that collectively influence the adaptation performance. Equation (4) precisely represents the first-order low-pass filter (LPF) with impulse response $\alpha e^{-\alpha t}$, where the input signal is denoted as $-(\mu/K_1K_2)(\partial d^2(t)/\partial w_k(t))$. In practical circuits, realizing an LPF is considerably more straightforward than implementing an integrator. The most basic form of an LPF can be achieved using an RC (resistor-capacitor) circuit. Combining (3) and (4) and assuming all components in the GALMS loop are linear, the weighting coefficient can be expressed as the

convolution of the LPF impulse response and the input signal, i.e.,

$$w_k(t) = \frac{2\mu\alpha}{K_1K_2}\int_0^t e^{-\alpha(t-\tau)}[r(\tau)-y(\tau)] \times \left\{[G_k(\tau)*X(\tau)]e^{j2\pi f_c\tau}\right\}d\tau \tag{5}$$

where K_1 and K_2 are the dimensional constants of the multipliers in the I/Q demodulator and modulator, respectively. α represents the decay constant of the LPF (where $\alpha = 1/RC$), and 2μ indicates the gain provided by the low noise amplifier (LNA). The operation of the GALMS loop can be outlined as follows: At the k-th tap, the baseband transmitted signal $X(t)$ is initially processed through the filter $G_k(t)$ and then up-converted to an RF reference signal. Then, this reference signal multiplies with the amplified looped-back signal at the I/Q demodulator. The outputs of this I/Q demodulator are filtered by the LPFs to produce the weighting coefficient $w_k(t)$, which subsequently modifies the reference signal at the I/Q modulator. The signals from all taps are accumulated to generate the cancellation signal $y(t)$. By subtracting $y(t)$ from the received signal $r(t)$, the desired signal $d(t)$ for the loop is obtained. This desired signal $d(t)$ is then fed back into the loop to recursively update the weighting coefficients until converging to a stable state.

To describe the GALMS loop convergence behavior, we first assume that the received signal $r(t)$, consisting of three components $z(t)$, $s(t)$, and $n(t)$, can be represented as

$$\begin{aligned} r(t) &= z(t)+s(t)+n(t) \\ &= \mathrm{Re}\left\{\left[Z(t)+S(t)+N(t)\right]e^{j2\pi f_c t}\right\} \end{aligned} \tag{6}$$

where $z(t)$ represents the SI from the local transmitter, $s(t)$ is the information-bearing signal, and $n(t)$ is the additive Gaussian noise. Correspondingly, $Z(t)$, $S(t)$, and $N(t)$ are the respective lowpass equivalent baseband signals. Furthermore, we model the SI channel using the same filter bank approach, allowing $Z(t)$ to be expressed as

$$Z(t) = \sum_{k=0}^{K-1} h_k^*[G_k(t)*X(t)] + \Delta Z(t) \tag{7}$$

where h_k is the k-th tap coefficient, $G_k(t)*X(t)$ can be considered as the associated basis function, and $\Delta Z(t)$ is the SI modeling error. By substituting (2), (6), and (7) into (5), we obtain the expression for the weighting coefficients $w_k(t)$ shown in (8). In deriving (8), we assume that the bandwidth of LPF is much narrower than the carrier frequency f_c, which ensures the complete elimination of signal components centered around $2f_c$ after the LPF.

Denoting the error between the k-th modeled tap coefficient of the interference channel and the k-th weighting coefficient of the adaptive filter as $u_k(t) = h_k - w_k(t)$, we can simplify (8) as

$$\begin{aligned} u_k(t) = h_k - \frac{\mu\alpha}{K_1K_2}\int_0^t e^{-\alpha(t-\tau)} \times \Bigg\{\Delta Z^*(\tau) + \sum_{k'=0}^{K-1} u_{k'}(\tau)[G_{k'}^*(\tau)*X^*(\tau)] \\ + S^*(\tau)+N^*(\tau)\Bigg\}[G_k(\tau)*X(\tau)]d\tau. \end{aligned} \tag{9}$$

III. STEADY-STATE ANALYSIS

The modeling error and the convergence of the residual interference power of the proposed GALMS loop can be examined through steady-state analysis. The combination of ensemble expectation and time averaging, denoted as $\bar{E}\{\cdot\}$, is employed. The normalized autocorrelation function of the baseband transmitted signal is expressed as

$$\begin{aligned} \Phi(\tau) &= \frac{1}{K_1K_2}\bar{E}\{X^*(t)X(t-\tau)\} \\ &= \frac{1}{K_1K_2T_s}\int_0^{T_s} E\{X^*(t)X(t-\tau)\}dt \\ &= \frac{1}{K_1K_2T_s}\int_{-\infty}^{\infty} p^*(t)p(t-\tau)dt. \end{aligned} \tag{10}$$

When the baseband transmitted signal $X(t)$ goes through two filters $G_k(t)$ and $G_{k'}(t)$, the normalized correlation coefficient

$$\begin{aligned} w_k(t) =& \frac{2\mu\alpha}{K_1K_2}\int_0^t e^{-\alpha(t-\tau)}Re\left\{\left[\Delta Z(\tau)+\sum_{k'=0}^{K-1}[h_{k'}^*-w_{k'}^*(\tau)][G_{k'}(\tau)*X(\tau)]+S(\tau)+N(\tau)\right]e^{j2\pi f_c\tau}\right\}[G_k(\tau)*X(\tau)]e^{j2\pi f_c\tau}d\tau \\ =& \frac{\mu\alpha}{K_1K_2}\int_0^t e^{-\alpha(t-\tau)}\Bigg\{\left[\Delta Z(\tau)+\sum_{k'=0}^{K-1}[h_{k'}^*-w_{k'}^*(\tau)][G_{k'}(\tau)*X(\tau)]+S(\tau)+N(\tau)\right]e^{j2\pi f_c\tau} \\ &+\left[\Delta Z^*(\tau)+\sum_{k'=0}^{K-1}[h_{k'}-w_{k'}(\tau)][G_{k'}^*(\tau)*X^*(\tau)]+S^*(\tau)+N^*(\tau)\right]e^{-j2\pi f_c\tau}\Bigg\}[G_k(\tau)*X(\tau)]e^{j2\pi f_c\tau}d\tau \\ =& \frac{\mu\alpha}{K_1K_2}\int_0^t e^{-\alpha(t-\tau)}\left[\Delta Z^*(\tau)+\sum_{k'=0}^{K-1}[h_{k'}-w_{k'}(\tau)][G_{k'}^*(\tau)*X^*(\tau)]+S^*(\tau)+N^*(\tau)\right][G_k(\tau)*X(\tau)]d\tau. \end{aligned} \tag{8}$$

between the two respective output signals is

$$\begin{aligned} R_{k,k'} &= \frac{1}{K_1K_2}\bar{E}\{[G_{k'}^*(t) * X^*(t)][G_k(t) * X(t)]\} \\ &= \frac{1}{K_1K_2}\int_{-\infty}^{\infty}\int_{-\infty}^{\infty} G_k(\tau)G_{k'}^*(\tau') \\ &\qquad \times \bar{E}\{X^*(t-\tau')X(t-\tau)\}d\tau d\tau' \\ &= \int_{-\infty}^{\infty}\int_{-\infty}^{\infty} G_k(\tau)G_{k'}^*(\tau')\Phi(\tau-\tau')d\tau d\tau'. \end{aligned} \tag{11}$$

A. Interference Channel Modeling

From (9), we can see that when the GALMS loop converges, i.e., $u_k(t) \to 0$, the weighting coefficient $w_k(t)$ approaches the corresponding tap coefficient h_k of the modeled SI channel. The regenerated SI, i.e., the cancellation signal $y(t)$, then approaches the modeled SI $\sum_{k=0}^{K-1} h_k^* G_k(t) * X(t)$. Consequently, if the modeled SI closely approximates the true SI $Z(t) = h^*(t) * X(t)$ where $h(t)$ is the true SI channel impulse response, better SI cancellation performance will be achieved. Therefore, SI channel modeling is crucial in SI cancellation circuits.

The modeled tap coefficients h_k of the SI channel can be determined by minimizing the normalized modeling error, which can be expressed as $\varepsilon^2 = (1/K_1K_2)\bar{E}\{|Z(t) - \sum_{k=0}^{K-1} h_k^* \int_{-\infty}^{\infty} G_k^*(\tau)X(t-\tau)d\tau|^2\}$. $\varepsilon^2 \to 0$ represents the ideal scenario for the modeled channels, implying that the GALMS loop can achieve desirable SI cancellation. To derive the modeled tap coefficients of the SI channel, we apply the principle of orthogonality, i.e.,

$$\begin{aligned} &\bar{E}\left\{\left[Z^*(t) - \sum_{k'=0}^{K-1} h_{k'}G_{k'}^*(t) * X^*(t)\right]G_k(t) * X(t)\right\} \\ &= 0, \qquad k = 0, 1, ..., K-1. \end{aligned} \tag{12}$$

Then, the modeled SI channel coefficients can be obtained as

$$\begin{aligned} \mathbf{h} &= \begin{bmatrix} h_0 \\ h_1 \\ \vdots \\ h_{K-1} \end{bmatrix} \\ &= \mathbf{R}^{-1}\begin{pmatrix} \int_{-\infty}^{\infty}\int_{-\infty}^{\infty} h(\tau)G_0(\tau')\Phi(\tau'-\tau)d\tau d\tau' \\ \int_{-\infty}^{\infty}\int_{-\infty}^{\infty} h(\tau)G_1(\tau')\Phi(\tau'-\tau)d\tau d\tau' \\ \vdots \\ \int_{-\infty}^{\infty}\int_{-\infty}^{\infty} h(\tau)G_{K-1}(\tau')\Phi(\tau'-\tau)d\tau d\tau' \end{pmatrix} \end{aligned} \tag{13}$$

where the correlation matrix is defined as

$$\mathbf{R} = \begin{pmatrix} R_{0,0} & R_{0,1} & \cdots & R_{0,K-1} \\ R_{1,0} & R_{1,1} & \cdots & R_{1,K-1} \\ \vdots & \vdots & \ddots & \vdots \\ R_{K-1,0} & R_{K-1,1} & \cdots & R_{K-1,K-1} \end{pmatrix}. \tag{14}$$

B. Frequency-Domain Representation of Modeled SI Channel

To better understand the importance of the spectral property of the filter bank in the GALMS loop, let us simplify the expressions in the evaluation of the correlation matrix, the modeled SI channel, and the modeling error.

First, we express the normalized correlation coefficient $R_{k,k'}$ in the frequency domain. By defining the Fourier transform pairs as $h(t) \iff \mathcal{H}(f)$, $X(t) \iff \mathcal{X}(f)$, $X^*(t) \iff \mathcal{X}^*(-f)$, $G_k(t) \iff \mathcal{G}_k(f)$, $G_k^*(t) \iff \mathcal{G}_k^*(-f)$, and $\Phi(t) \iff \Phi(f)$, (11) can be expressed as

$$\begin{aligned} R_{k,k'} &= \int_{-\infty}^{\infty}\int_{-\infty}^{\infty} G_k(\tau)G_{k'}^*(\tau')\Phi(\tau'-\tau)d\tau d\tau' \\ &= \int_{-\infty}^{\infty}\int_{-\infty}^{\infty}\left[\int_{-\infty}^{\infty}\mathcal{G}_k(f)e^{j2\pi f\tau}df\int_{-\infty}^{\infty}\mathcal{G}_{k'}^*(f')e^{-j2\pi f'\tau}df'\right. \\ &\qquad \left.\times\int_{-\infty}^{\infty}\Phi(f'')e^{-j2\pi f'(\tau'-\tau)}df''\right]d\tau d\tau' \\ &= \int_{-\infty}^{\infty}\int_{-\infty}^{\infty}\int_{-\infty}^{\infty}\left[\mathcal{G}_k(f)\mathcal{G}_{k'}^*(f')\Phi(f'')\right] \\ &\qquad \times\left[\int_{-\infty}^{\infty}e^{j2\pi(f-f'')\tau}d\tau\int_{-\infty}^{\infty}e^{j2\pi(f''-f')\tau'}d\tau'\right]df\,df'\,df'' \\ &= \int_{-\infty}^{\infty}\int_{-\infty}^{\infty}\int_{-\infty}^{\infty}\mathcal{G}_k(f)\mathcal{G}_{k'}^*(f')\Phi(f'') \\ &\qquad \times\left[\delta(f-f'')\delta(f''-f')\right]df\,df'\,df''. \end{aligned} \tag{15}$$

To simplify (15), we utilize the sifting property of the Dirac delta function, which reduces the dimensionality of integrals by evaluating only the integrand at the zeros of the delta functions. The original triple integral involves integrands multiplied by two Dirac delta functions, $\delta(f-f'')$ and $\delta(f''-f')$, which effectively constrain the integration to the locus of points where $f = f' = f''$. Applying these constraints, the triple integral over f, f', and f'' can be reduced to a single integral over f. This reduction simplifies (15) to a one-dimensional integral of the product of the functions $\mathcal{G}_k(f)$, $\mathcal{G}_{k'}^*(f)$, and $\Phi(f)$ as

$$R_{k,k'} = \int_{-\infty}^{\infty}\mathcal{G}_k(f)\mathcal{G}_{k'}^*(f)\Phi(f)df. \tag{16}$$

Equation (16) is more analytically tractable and provides deeper insight into the frequency domain interactions within the system. Similarly, we can obtain the modeled tap coefficients shown in the frequency domain as

$$\mathbf{h} = \begin{bmatrix} h_0 \\ h_1 \\ \vdots \\ h_{K-1} \end{bmatrix} = \mathbf{R}^{-1}\begin{pmatrix} \int_{-\infty}^{\infty}\mathcal{H}(f)\mathcal{G}_0(f)\Phi(f)df \\ \int_{-\infty}^{\infty}\mathcal{H}(f)\mathcal{G}_1(f)\Phi(f)df \\ \vdots \\ \int_{-\infty}^{\infty}\mathcal{H}(f)\mathcal{G}_{K-1}(f)\Phi(f)df \end{pmatrix}. \tag{17}$$

Based on the frequency domain representation discussed above, the modeling error is finally expressed as (18), where $\{\cdot\}^H$ denotes transposition and conjugation. In deriving (18), we have also invoked the property $R_{k,k'}^* = R_{k',k}$.

$$
\begin{aligned}
\varepsilon^2 &= \frac{1}{K_1K_2}\bar{E}\left\{\left[Z(t)-\sum_{k=0}^{K-1}h_k^*\int_{-\infty}^{\infty}G_k(\tau)X(t-\tau)d\tau\right]^2\right\}\\
&= \frac{1}{K_1K_2}\bar{E}\left\{\left[\int_{-\infty}^{\infty}h^*(\tau')X(t-\tau')d\tau'-\sum_{k=0}^{K-1}h_k^*\int_{-\infty}^{\infty}G_k(\tau')X(t-\tau')d\tau'\right]^*\left[\int_{-\infty}^{\infty}h^*(\tau)X(t-\tau)d\tau\right]\right\}\\
&= \int_{-\infty}^{\infty}\int_{-\infty}^{\infty}h^*(\tau)h(\tau')\Phi(\tau-\tau')d\tau'd\tau-\sum_{k=0}^{K-1}h_k\int_{-\infty}^{\infty}\int_{-\infty}^{\infty}h^*(\tau)G_k(\tau')\Phi(\tau-\tau')d\tau d\tau'\\
&= \int_{-\infty}^{\infty}\int_{-\infty}^{\infty}h^*(\tau)h(\tau')\Phi(\tau-\tau')d\tau'd\tau-\begin{pmatrix}\int_{-\infty}^{\infty}\int_{-\infty}^{\infty}h(\tau)G_0(\tau')\Phi(\tau'-\tau)d\tau d\tau'\\ \int_{-\infty}^{\infty}\int_{-\infty}^{\infty}h(\tau)G_1(\tau')\Phi(\tau'-\tau)d\tau d\tau'\\ \vdots\\ \int_{-\infty}^{\infty}\int_{-\infty}^{\infty}h(\tau)G_{K-1}(\tau')\Phi(\tau'-\tau)d\tau d\tau'\end{pmatrix}^H\mathbf{h}\\
&= \int_{-\infty}^{\infty}|\mathcal{H}(f)|^2\Phi(f)df-\mathbf{h}^H\mathbf{R}\mathbf{h}.
\end{aligned}
\tag{18}
$$

C. Convergence of Residual Interference Power

Residual interference power is critical for assessing the GALMS loop's performance across various filter structures. Ideally, the residual interference power should be zero. However, as shown in (9), the weighting coefficient error is affected by various factors, such as the SI modeling error, the desired remote signal, and the receiver noise. Therefore, further analysis is necessary to determine the residual interference power after the GALMS loop converges. The normalized residual interference power can be expressed as (19) below.

From (19), it can be observed that the residual interference power $P_{RI}(t)$ is related to three factors. These factors are the SI modeling error ε^2, the weighting coefficient error $u_k(t)$ between the tap coefficients and weighting coefficients, and the correlation coefficients $R_{k,k'}$. Based on the independence assumption and the principle of orthogonality in (12), taking both the ensemble expectation and time averaging on (9), we have

$$
\bar{\bar{u}}_k(t) = h_k-\mu\alpha\int_0^t e^{-\alpha(t-\tau)}\sum_{k'=0}^{K-1}\bar{\bar{u}}_{k'}(\tau)R_{k,k'}d\tau, \tag{20}
$$

or, in matrix form

$$
\bar{\bar{\mathbf{u}}}(t) = \mathbf{h}-\mu\alpha\int_0^t e^{-\alpha(t-\tau)}\mathbf{R}\bar{\bar{\mathbf{u}}}(t)\,d\tau. \tag{21}
$$

Equation (21) has the same form as [23, Eq. (26)] but different correlation matrix $\mathbf{R}$. Therefore, following the same steps in [23], which are provided in Appendix A, we can derive the theoretical value of the residual interference power shown in (22). It can be seen from (22) that the residual SI power obtained by the GALMS loop can be estimated by its loop

$$
\begin{aligned}
P_{RI}(t) &= \frac{1}{K_1K_2}\bar{E}\{[z(t)-y(t)]^2\} = \frac{1}{K_1K_2}\bar{E}\left\{\left[Re\left\{\left[Z(t)-\sum_{k=0}^{K-1}h_k^*[G_k*X(t)]+\sum_{k=0}^{K-1}u_k^*(t)[G_k*X(t)]\right]e^{j2\pi f_c t}\right\}\right]^2\right\}\\
&= \frac{1}{2K_1K_2}\bar{E}\left\{\left[Z(t)-\sum_{k=0}^{K-1}h_k^*[G_k*X(t)]+\sum_{k=0}^{K-1}u_k^*(t)[G_k*X(t)]\right]^2\right\}\\
&= \frac{1}{2K_1K_2}\bar{E}\left\{\left|Z(t)-\sum_{k=0}^{K-1}h_k^*[G_k*X(t)]\right|^2\right\}+\frac{1}{2K_1K_2}\bar{E}\left\{\left|\sum_{k=0}^{K-1}u_k^*(t)[G_k*X(t)]\right|^2\right\}\\
&= \frac{1}{2}\varepsilon^2+\frac{1}{2K_1K_2}\bar{E}\left\{\sum_{k=0}^{K-1}u_k^*(t)[G_k*X(t)]\times\sum_{k'=0}^{K-1}u_{k'}(t)[G_{k'}^**X^*(t)]\right\}\\
&= \frac{1}{2}\varepsilon^2+\frac{1}{2K_1K_2}\bar{E}\left\{\sum_{k=0}^{K-1}\sum_{k'=0}^{K-1}u_k^*(t)\bar{E}\{[G_k*X(t)]\times[G_{k'}^**X^*(t)]\}u_{k'}(t)\right\}\\
&= \frac{1}{2}\varepsilon^2+\frac{1}{2}\bar{E}\left\{\sum_{k=0}^{K-1}\sum_{k'=0}^{K-1}u_k^*(t)R_{k,k'}u_{k'}(t)\right\}.
\end{aligned}
\tag{19}
$$

parameters, such as the loop gain μ, the eigenvalues of $\mathbf{R}$ and the SI channel modeling error ε^2.

IV. SIMULATION RESULTS

In this section, we focus on the simulation verification of the theoretical results presented in Section III and compare the proposed GALMS structure to the conventional ALMS loop. We begin by determining the simulation parameters and introducing some typical examples of the generalized filter bank, including tapped DL, bandpass filter (BPF), and allpass filter (APF). Subsequently, we comprehensively compare and discuss the modeling error ε^2 associated with the above three structures. We also examine the residual interference power $P_{RI}(t)$ to show the convergence after passing through the GALMS loop.

The system simulation uses quadrature phase shift keying modulation (QPSK) for a single carrier system with $T_s = 1$ ns symbol duration. We employ a root-raised cosine filter with a roll-off factor of $\beta = 0.25$ for pulse shaping, which generates a stationary raised-cosine autocorrelation function. The LNA provides a gain of 26 dB (i.e., $\mu = 10$), and the carrier frequency is set at 76 GHz. The LPF constant in the GALMS loop is set to $\alpha T_s = 1.7655 \times 10^{-5}$. The transmitted signal maintains a consistent power level of 0 dBm across a 50 Ω load, corresponding to a power level of 17 dBm (10log(50)) for a 1 Ω load. Therefore, the mean squared amplitude of the transmitted signal for a 1 Ω load is given by $V_X^2 = 2 \times 10^{(17-30)/10} = 0.1\ V^2$. Dimensional constants for the multipliers are fixed at $K_1 K_2 = 0.001\ V^2$. The SI power is 25 dB lower than the transmitted signal. The combined power of the received signal, which includes both remote transmission and thermal noise, is 60 dB below the SI level.

A. Three Different Filter Bank Structures

1) Tapped DL: Since a conventional tapped DL adaptive filter is a special case of the GALMS loop, simulating the GALMS loop with the tapped DL in its filter bank can be used as a benchmark for comparison. The tapped DL consists of sequentially arranged delay elements, each corresponding to a 'tap'. Every tap imposes a distinct delay on the input signal, creating several delayed replicas of the original signal. These taps can then be merged or manipulated to fulfill certain signal processing goals. Mathematically, the impulse response of each tap in a tapped DL can be expressed as $G_k(t) = \delta(t - kT)$, where T is the delay time. The phase response is $\angle \mathcal{G}_k(f) = -2\pi f T$, indicating that the tapped DL introduces a linear phase shift to the transmitted signal.

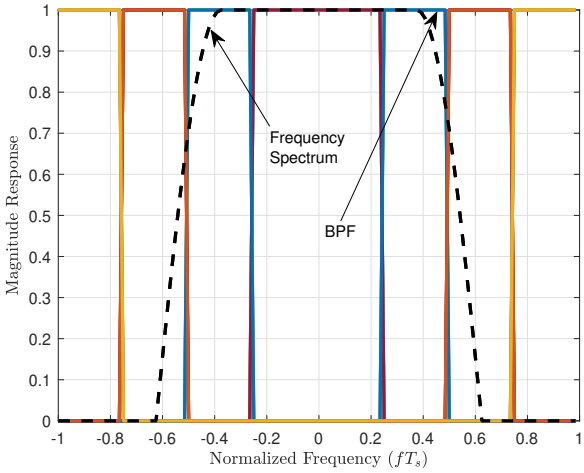

Fig. 3. Frequency spectrum of the transmitted signal and magnitude response of 8 BPFs.

2) BPF Bank: BPF bank decomposes the transmitted signal into multiple reference signals occupying different partials of the signal spectrum. The number of taps determines the bandwidth of each frequency band so that combining all the taps will cover the whole signal spectrum. The larger the number of taps, the narrower the bandwidth of each BPF, allowing for finer frequency decomposition resolution. This paper uses the ideal BPFs with the raised-cosine response for frequency decomposition. This offers a theoretically viable solution to minimize the significant impact of the group delay of the analog BPF on the signal phase to the greatest extent possible. Fig. 3 demonstrates the decomposition of a transmitted signal's frequency spectrum using a bank of 8 ideal BPFs with equally spaced center frequencies. These filters are designed with a raised-cosine response characterized by a roll-off factor. The purpose of employing multiple BPFs is to partition the transmitted signal into several reference signals, with each filter isolating a distinct portion of the overall spectrum.

3) APF Bank: An APF in signal processing maintains a uniform magnitude response across frequencies while introducing variable phase shifts. It is used for phase equalization, audio effects, communication systems, and frequency discrimination, enabling precise phase adjustments without altering signal magnitudes. The first-order APF transfer function can

$$
\begin{aligned}
P_{RI}(t) =& \frac{1}{2}\varepsilon^2 + \frac{1}{2}\mathbf{h}^H \mathbf{Q}\, \mathrm{diag}\left\{ (\lambda_k - \bar{\lambda}) \left(\frac{1}{1+\mu\lambda_k} + \frac{\mu\lambda_k}{1+\mu\lambda_k} e^{-(1+\mu\lambda_k)\alpha t} \right)^2 \right. \\
& \left. + \frac{\bar{\lambda}}{(1+\mu\lambda_k)^2} + \frac{2\mu\lambda_k\bar{\lambda}}{(1+\mu\lambda_k)^2} e^{-(1+\mu\lambda_k)\alpha t} + \frac{\mu^2\lambda_k^2\bar{\lambda}}{(1+\mu\lambda_k)^2} e^{-2(1+\mu\lambda_k)\alpha t} - \bar{\lambda} e^{-2(1+\mu\bar{\lambda})\alpha t} \right\} \mathbf{Q}^{-1}\mathbf{h} \\
=& \frac{1}{2}\varepsilon^2 + \frac{1}{2}\mathbf{h}^H \mathbf{Q}\, \mathrm{diag}\left\{ \frac{\lambda_k}{(1+\mu\lambda_k)^2} + \frac{2\mu\lambda_k^2}{(1+\mu\lambda_k)^2} e^{-(1+\mu\lambda_k)\alpha t} + \frac{\mu^2\lambda_k^3}{(1+\mu\lambda_k)^2} e^{-2(1+\mu\lambda_k)\alpha t} - \bar{\lambda} e^{-2(1+\mu\bar{\lambda})\alpha t} \right\} \mathbf{Q}^{-1}\mathbf{h}.
\end{aligned}
\tag{22}
$$

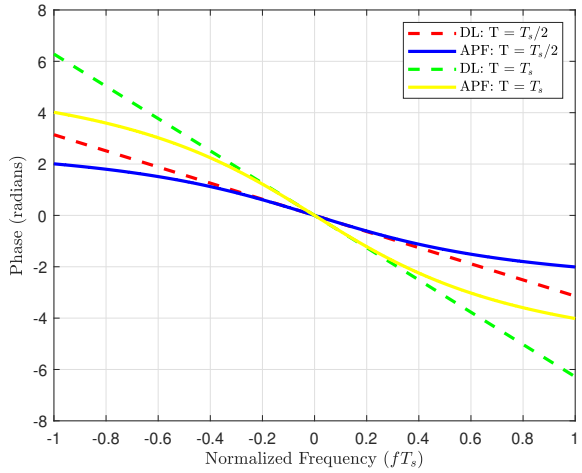

Fig. 4. Phase response comparison of tapped DLs and APFs.

be expressed as

$$H(s) = (-1)\frac{s-\omega_0}{s+\omega_0} \tag{23}$$

where s is the complex frequency domain parameter and ω_0 is the characteristic angular frequency. The transfer function of the k-th order APF can be expressed as

$$\begin{aligned} H^{(k)}(s) &= \left(\frac{\omega_0 - s}{\omega_0 + s}\right)^k = \left(\frac{2\omega_0}{s+\omega_0} - 1\right)^k \\ &= \sum_{k'=0}^{k} \binom{k}{k'} \left(\frac{2\omega_0}{s+\omega_0}\right)^{k'} (-1)^{k-k'}. \end{aligned} \tag{24}$$

According to the binomial theorem and inverse Laplace transform, the impulse response of the k-th order APF $H^{(k)}(s)$ in the time domain can be represented as

$$\begin{aligned} h^{(k)}(t) &= \mathcal{L}^{-}[H^{(k)}(s)] = (-1)^k \delta(t) \\ &+ \sum_{k'=1}^{k} \binom{k}{k'} \frac{(2\omega_0)^{k'} t^{k'-1} e^{-\omega_0 t}}{(k'-1)!} (-1)^{k-k'}. \end{aligned} \tag{25}$$

Detailed derivations of (25) are provided in Appendix B. Defining $G_k(t) = h^{(k)}(t)$, the phase response of the k-th order APF is $\angle \mathcal{G}_k(f) = -2k\arctan(2\pi f/\omega_0)$. This indicates a nonlinear phase shift that varies with frequency, causing the filter to apply different delays to different signal frequency components.

In Fig. 4, we present a comparative analysis of the phase responses between the tapped DL with delay T and the first-order APF with $w_0 = 2/T$ at two delays: $T = T_s/2$ and $T = T_s$. The tapped DL exhibits a linear phase shift across the frequency spectrum represented by the dashed red and green lines for $T = T_s/2$ and $T = T_s$, signifying a uniform delay irrespective of frequency. On the other hand, the first-order APF demonstrates a nonlinear phase response depicted by the solid blue and yellow lines for $T = T_s/2$ and $T = T_s$, respectively, indicating intricate frequency-dependent phase modification. The steeper phase response curves at $T = T_s$ highlight the direct relationship between delay and phase shift:

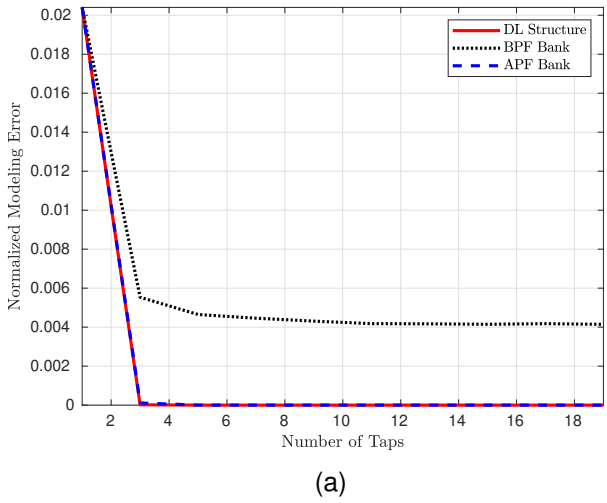

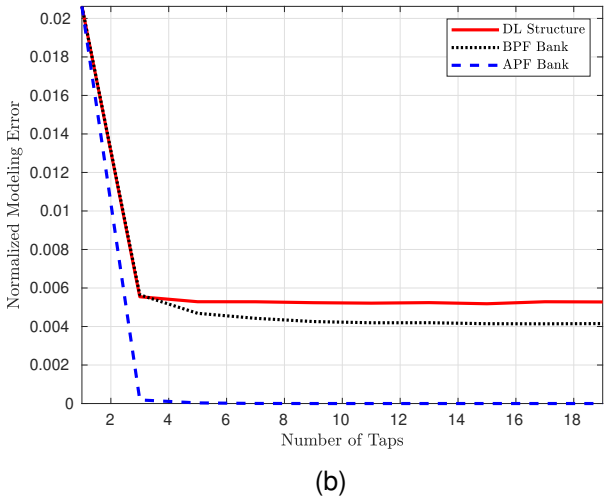

Fig. 5. Normalized modeling error of the GALMS loops with 3 types of filter banks for different tapped spacing scenarios: (a) $T_s/2$ spacing, (b) T_s spacing.

a larger delay results in a proportionally greater phase shift at any given frequency. The phase response of the APF aligns with the tapped delay's slope of phase change, also known as the group delay. The APF and the tapped DL introduce an identical phase shift only at $f = 0$ when they have the same group delay T. As the frequency increases, the phase shift of the APF continuously decreases and eventually stabilizes. As the delay decreases, the phase response curve of the APF closely approximates that of the tapped DL, which means that the APF increasingly resembles a tapped DL for a smaller delay.

B. Modelling Error Simulation Analysis

In simulating the impact of various filter structures on the modeling error, we employ an interference channel $h(t)$ characterized by an exponentially distributed power profile with the root mean square delay spread selected as $\sigma = KT_s/6$. The interference channel consists of $K = 5$ taps spaced equally at $T_s/2$. The averaged modeling error for the GALMS loops

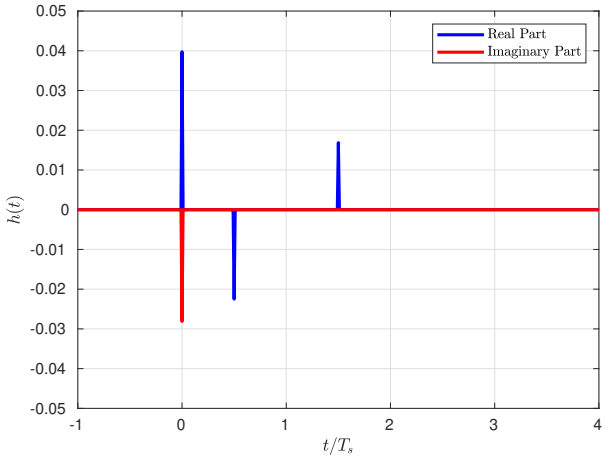

Fig. 6. SI channel impulse response for residual power simulation.

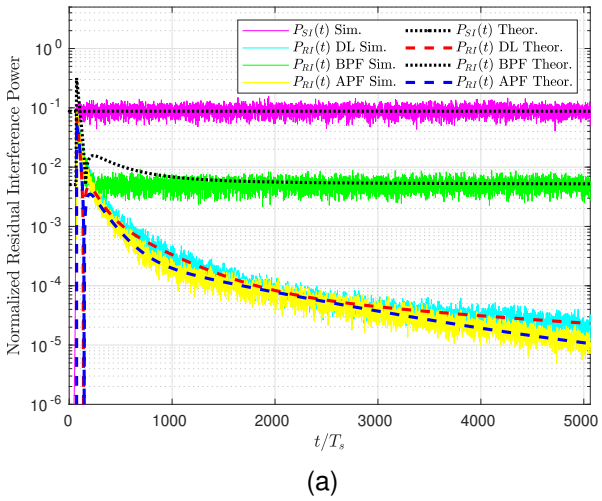

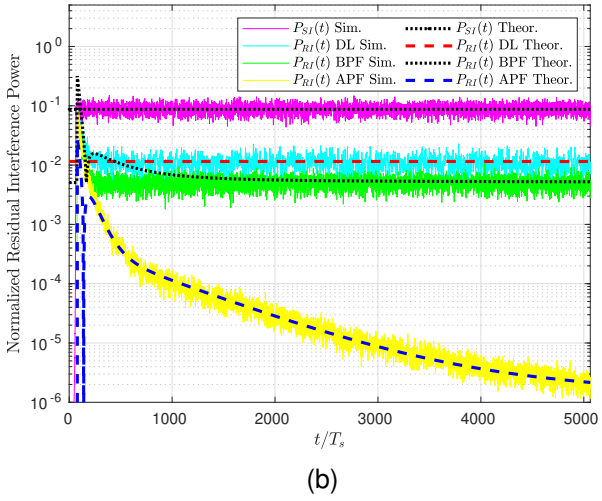

Fig. 7. Normalized residual interference power for GALMS loop with 16 taps: (a) $T_s/2$ spacing, (b) T_s spacing.

with different filter banks is obtained over 1000 realizations of the SI channel.

Fig. 5 depicts the normalized modeling error associated with 3 distinct filter bank structures under different tapped spacing scenarios. Fig. 5(a) depicts the modeling error when tapped spacings in the tapped DL and the APF are both $T_s/2$. Notably, the GALMS loop with APF and tapped DL structures have almost the same performance, with the modeling error approaching 0 when more than 3 taps are used. Meanwhile, the case of the BPF demonstrates an overall performance inferiority compared to the former two structures. The normalized modeling error of the BPF bank is solely relative to the number of taps employed and does not depend on the tapped spacing.

In Fig. 5(b), at the T_s tapped spacing, it becomes apparent that the APF bank exhibits superior performance compared to the tapped DL structure. When the number of filters exceeds 5, the normalized modeling error for the APF bank can still approach zero. In contrast, the modeling error with the tapped DL structure can only reach 5.4×10^{-3}, which is even higher than that of the BPF bank. This is because the tapped DL structure with T_s tapped spacing violates the Nyquist Theorem, preventing it from mimicking the SI channel accurately. However, due to the unique phase characteristics of the APFs, the APF bank can still model the SI channel well. Therefore, it performs better than the tapped DL structure at the T_s tapped spacing.

C. Residual Interference Power Simulation

One instance of the SI channel with the impulse response given by $h(t) = 10^{-25/20}\left(\frac{\sqrt{2}}{2} - 0.5j\right)\delta(t) - 0.4\delta(t - 0.5T_s) + 0.3\delta(t - 1.5T_s)$, as illustrated in Fig. 6, is used for residual interference power analysis. The SI channel comprises three paths: the first path corresponds to the direct coupling between the transmit and receive antennas, while the second and third paths are reflections from surrounding obstacles, introducing delays of $0.5T_s$ and $1.5T_s$, respectively. Due to the propagation domain SI suppression, the SI power is scaled down by 25 dB relative to the transmitted signal power. Fig. 7 presents the normalized residual powers for three different filter structures, each with 16 taps in the loop, compared at tapped spacings of $T_s/2$ and T_s, respectively. The instant SI power, denoted as $P_{SI}(t)$ shown in Fig. 7, has the average value calculated as $\int_{-\infty}^{\infty} |\mathcal{H}(f)|^2 \Phi(f)\, df$. Fig. 7(a) reveals that the APF bank and the tapped DL structure with $T_s/2$ tapped spacing perform similarly, achieving above 45 dB of SI cancellation.

When the tapped spacing is T_s, the GALMS loop with the APF bank significantly outperforms the conventional tapped DL structure, as shown in Fig. 7(b). The level of SI cancellation obtained by the former is about 56 dB, while that of the latter is only about 10 dB. The residual interference power curve of the BPF bank remains unchanged because the effectiveness of the BPF bank is solely dependent on the number of taps rather than the temporal spacing in the time domain. The theoretical residual powers calculated by (22) match the corresponding simulation curves, proving the steady-state analyses conducted in Section III.

To investigate the impact of the number of taps on the

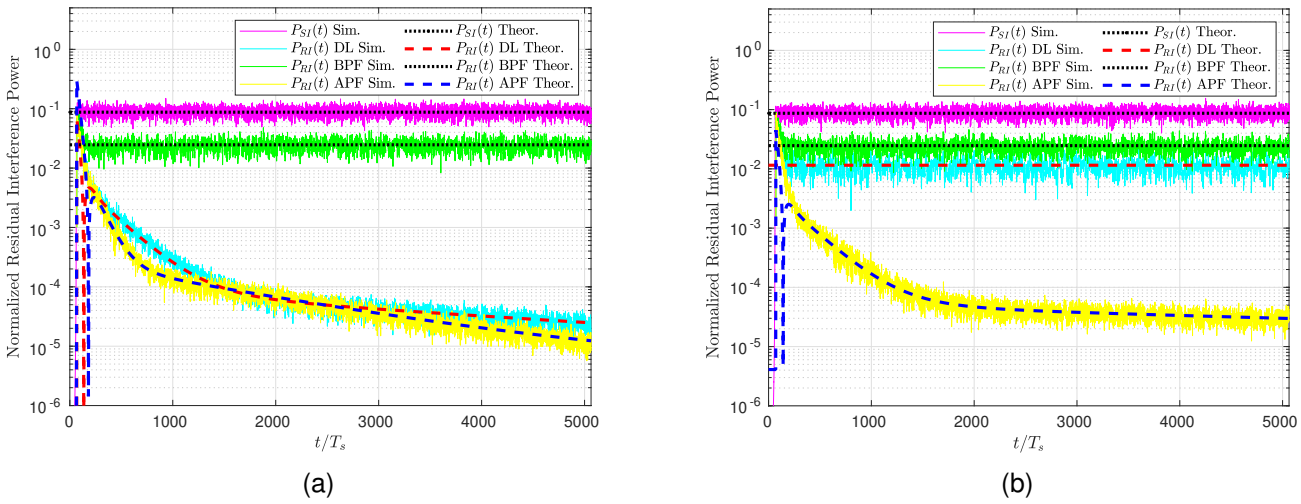

Fig. 8. Normalized residual interference power for GALMS loop with 8 taps: (a) $T_s/2$ spacing, (b) T_s spacing.

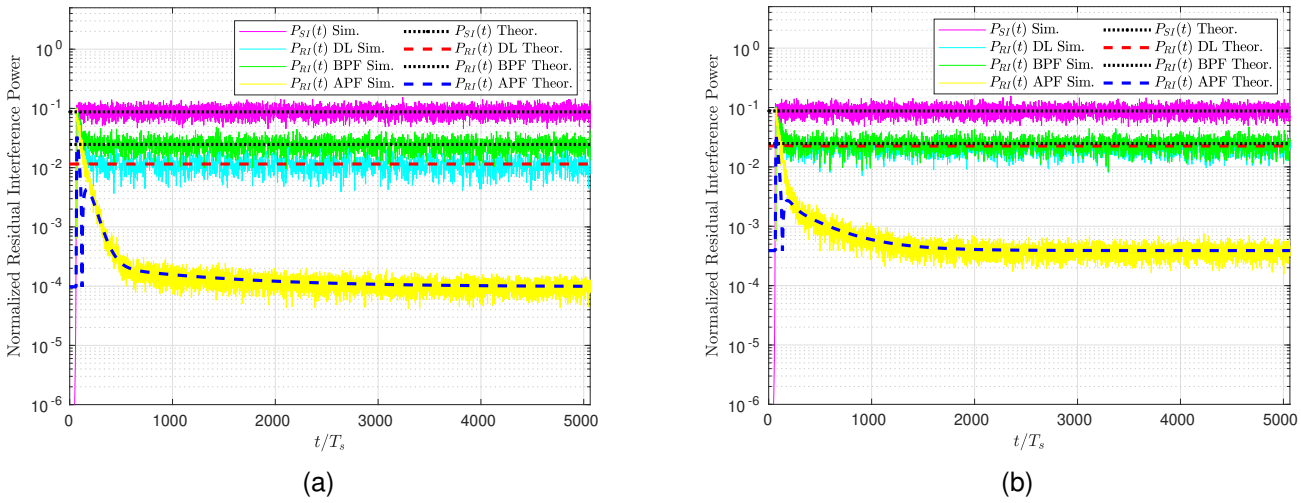

Fig. 9. Normalized residual interference power for GALMS loop with 6 taps: (a) T_s spacing, (b) $1.25T_s$ spacing.

SI cancellation performance, we simulate the GALMS loop with 8 taps, as shown in Fig. 8. Comparing the residual power of the APF bank in Fig. 8(b) with that of the tapped DL structure in Fig. 7(a), it is evident that by increasing tapped spacing and reducing the number of taps, the proposed GALMS loop structure with APF bank can still achieve similar SI cancellation performance as the tapped DL structure with double number of taps. This indicates that we do not have to rely on the conventional tapped DL structure when designing adaptive filters. The proposed GALMS loop can be an excellent alternative for significantly reducing implementation difficulty and circuit complexity in IBFD systems. It is worth noting that, as the filter bank in the proposed GALMS loop is implemented at baseband, one additional mixer is necessary to up-convert the reference signal for each tap to RF, which indeed increases the complexity for the same number of taps as compared with tapped DL structure directly implemented at RF. However, as the GALMS loop has the capability to reduce the number of taps significantly for some applications, such as mm-wave communications, the overall complexity can still be lower than that of the conventional approaches.

D. Case Study

To illustrate the effectiveness of our proposed method, we present a case study focusing on a typical mm-wave communication scenario. Considering the same mm-wave system configuration described earlier and assuming the surrounding obstacles are within close proximity to the IBFD transceiver, the SI signal can be modeled as outlined in Section IV.C. At the operating temperature of $25\,^{\circ}\mathrm{C}$, the thermal noise of this system can be calculated as $10\log\left[1.38\times10^{-23}\times(273.15+25)\times\left(\frac{1}{T_s}\right)\right]+30\approx-84\,\mathrm{dBm}$. Next, assuming that the receiver employs a 10-bit ADC with an effective number of 8 bits, the effective dynamic

TABLE I
COMPARISON WITH EXISTING SI CANCELLATION TECHNIQUES

Metrics \ Literature	[5]	[16]	[23]	[31]	[36]	This Work
Analog or Digital Domain	Digital	Digital	Analog	Analog	Analog	Analog
No Tapped DL Required	✗	✗	✗	✗	✗	✓
No DSP Required	✗	✗	✓	✗	✗	✓
Theoretical Analysis	✓	✓	✓	✓	✓	✓
Suitability for mm-wave Applications	✓	✗	✓	✗	✗	✓
Quantization Noise[1]Analysis	✗	✓	N/A	✗	✗	N/A
Scalability to Wider Bandwidth	✗	✓	✓	✗	✓	✓
Adaptability to Rapid SI Channel Changes	✗	✗	✓	✗	✗	✓
Level of SI Cancellation (dB)	≈ 28	≈ 60	≈ 40	≈ 38	≈ 30	> 45

[1] Quantization noise is only applicable for structures that require DSP and DAC.

range of the ADC can be calculated as $6 \times 8 = 48$ dB. For the IBFD system to function correctly, the received signal at the ADC input must be below $-84 + 48 = -36$ dBm. Given the transmit signal power of 20 dBm and the propagation domain isolation of 25 dB, the RF domain cancellation must achieve more than 31 dB to bring the SI signal within the dynamic range of the ADC for further digital domain SI cancellation.

From the level of SI cancellation required and the results presented in Fig. 8(a), both the tapped DL and the GALMS with APF bank can satisfy the target when 8 taps and $T_s/2$ spacing are used. However, accurately delaying the mm-wave signal at sub-nanosecond levels in analog circuitry is challenging. Therefore, a signal delay exceeding one nanosecond is preferable, only the GALMS loop with APF bank can reach the threshold with T_s spacing. Further simulations are conducted with 6 taps and tap spacings of T_s and $1.25T_s$. The results in Fig. 9 confirm that the GALMS loop surpasses the SI cancellation threshold with fewer taps for both T_s and $1.25T_s$ spacings. Additionally, reducing the number of taps decreases the total number of required mixers, leading to lower hardware complexity.

E. Comparison With Existing Approaches

Table I presents a comparison of the proposed GALMS loop with several existing approaches [5], [16], [23], [31], [36]. Our method distinguishes itself by implementing tap weight control directly at the RF level, which eliminates the need for a DSP model. Rather than relying solely on the conventional tapped DL structure, an alternative filter bank is adopted to obtain a significant level of SI cancellation while reducing the number of taps required. Additionally, the proposed GALMS loop can be used for mm-wave communications, which other methods may not be suitable due to the overwhelming number of taps required.

In our future work, we will explore modifications to the GALMS loop structure to address non-linear SI signals within the digital domain. This includes evaluating the impact of quantization noise, ensuring scalability to wider bandwidths, and enhancing adaptability to rapid changes in the SI channel. Additionally, we aim to develop strategies that optimize the loop's performance across various operating conditions to ensure its robust and efficient SI cancellation.

V. CONCLUSION

In this paper, we propose a GALMS loop structure as a promising solution for analog SI cancellation in wideband IBFD systems. We present comprehensive analyses to derive the modeling error and residual SI power associated with the proposed structure. Simulations are conducted to evaluate and compare the proposed GALMS loop utilizing different adaptive filter structures. The results show that the GALMS loop equipped with the APF bank significantly outperforms the conventional ALMS loop when the tapped spacing in the adaptive filter is wider than the Nyquist period. Consequently, the number of taps required in the GALMS structure can be reduced while achieving comparable levels of SI cancellation. This suggests that the GALMS structure offers a valuable alternative for reducing complexity in wideband IBFD systems.

APPENDIX A
SOLUTION FOR THE THEORETICAL VALUE OF RESIDUAL INTERFERENCE POWER

In (21), the vector $\bar{\bar{\mathbf{u}}}(t)$ can be expressed as

$$\bar{\bar{\mathbf{u}}}(t) = \begin{bmatrix} \bar{\bar{u}}_0(t) \\ \bar{\bar{u}}_1(t) \\ \vdots \\ \bar{\bar{u}}_{K-1}(t) \end{bmatrix}$$

where $\bar{\bar{u}}_k = \bar{E}\{u_k(t)\}$. The autocorrelation matrix $\mathbf{R}$, being a square matrix with linearly independent eigenvectors, can be decomposed by eigendecomposition $\mathbf{R} = \mathbf{Q}\mathbf{\Lambda}\mathbf{Q}^{-1}$, the columns of $\mathbf{Q}$ are the corresponding eigenvectors of $\mathbf{R}$, and $\mathbf{\Lambda}$ is a diagonal matrix formed by the eigenvalues of $\mathbf{R}$, i.e.,

$$\mathbf{\Lambda} = \begin{bmatrix} \lambda_0 & 0 & \cdots & 0 \\ 0 & \lambda_1 & \cdots & 0 \\ \vdots & \vdots & \ddots & \vdots \\ 0 & 0 & \cdots & \lambda_{K-1} \end{bmatrix}.$$

Then, (21) can be rewritten as

$$\bar{\bar{\mathbf{v}}}(t) = \mathbf{g} - \mu\alpha \int_0^t e^{-\alpha(t-\tau)} \mathbf{\Lambda} \bar{\bar{\mathbf{v}}}(\tau) d\tau \tag{26}$$

where $\bar{\bar{\mathbf{v}}}(t) = \mathbf{Q}^{-1}\bar{\bar{\mathbf{u}}}(t)$ and $\mathbf{g} = \mathbf{Q}^{-1}\mathbf{h}$. The orthonormal modal matrix $\mathbf{Q}$ satisfies the condition that its transpose is equal to its inverse, i.e. $\mathbf{Q}^H = \mathbf{Q}^{-1}$. $R_{k,k}$ can be represented as average eigenvalue. i.e., $R_{k,k} = (1/K)\sum_{k=0}^{K-1}\lambda_k = \bar{\lambda}$. Rewrite (26) in the form of an integral equation with a single element as

$$\bar{\bar{v}}_k(t) = g_l - \mu\lambda_k\alpha \int_0^t e^{-\alpha(t-\tau)} \bar{\bar{v}}_k(\tau) d\tau, \quad k = 0, 1, \ldots, K-1 \tag{27}$$

where g_k is the kth element of $\mathbf{g}$ column vector.

To solve for $\bar{\bar{v}}_k(t)$, we can utilize Laplace transform and the properties of convolution based on (27). The Laplace transform of $\bar{\bar{v}}_k(t)$ is given by $\bar{\bar{V}}_k(s) = g_k(1/s) - \mu\lambda_k(\alpha/(s+\alpha))\bar{\bar{V}}_k(s)$, which can be simplified as

$$\begin{aligned} \bar{\bar{V}}_k(s) &= \frac{g_k \frac{1}{s}}{1 + \lambda_k \frac{\alpha}{s+\alpha}} \\ &= \frac{(s+\alpha)g_k}{s^2 + (1+\mu\lambda_k)\alpha s} \\ &= \frac{g_k}{1+\mu\lambda_k}\frac{1}{s} + \frac{\mu\lambda_k}{1+\mu\lambda_k}\frac{g_k}{s + (1+\mu\lambda_k)\alpha}. \end{aligned} \tag{28}$$

Performing the inverse Laplace transform on $\bar{\bar{V}}_k(s)$, $\bar{\bar{v}}_k(t)$ is obtained as

$$\bar{\bar{v}}_k(t) = \frac{g_k}{1+\mu\lambda_k} + \frac{\mu\lambda_k g_k}{1+\mu\lambda_k} e^{-(1+\mu\lambda_k)\alpha t}, \quad t > 0. \tag{29}$$

Then, $\bar{\bar{\mathbf{u}}}(t)$ is solved as

$$\begin{aligned} \bar{\bar{\mathbf{u}}}(t) &= \mathbf{Q}\bar{\bar{\mathbf{v}}}(t) \\ &= \mathbf{Q} diag\left\{ \frac{1}{1+\mu\lambda_k} + \frac{\mu\lambda_k}{1+\mu\lambda_k} e^{-(1+\mu\lambda_k)\alpha t} \right\} \mathbf{g} \\ &= \mathbf{Q} diag\left\{ \frac{1}{1+\mu\lambda_k} + \frac{\mu\lambda_k}{1+\mu\lambda_k} e^{-(1+\mu\lambda_k)\alpha t} \right\} \mathbf{Q^{-1}h} \end{aligned} \tag{30}$$

where $diag\{\cdot\}$ refers to a diagonal matrix, and each diagonal element is defined by a function of its position, k.

Let's assume that $u_k(t), k = 0, 1, \ldots, K-1$, are mutually independent. We can simplify the residual interference power (19) as

$$\begin{aligned} P_{RI}(t) &= \frac{1}{2}\varepsilon^2 + \frac{1}{2}\left\{ \sum_{k=0}^{K-1} \sum_{k'=0, k'\neq k}^{K-1} u_k^*(t) R_{k,k'} u_{k'}(t) \right. \\ &\qquad \left. + R_{k,k} \sum_{k=0}^{K-1} |u_k(t)|^2 \right\} \\ &= \frac{1}{2}\varepsilon^2 + \frac{1}{2} \sum_{k=0}^{K-1} \sum_{k'=0, k'\neq k}^{K-1} \bar{\bar{u}}_k^*(t) R_{k,k'} \bar{\bar{u}}_{k'}(t) \\ &\qquad + \frac{1}{2} R_{k,k} \sum_{k=0}^{K-1} \bar{\bar{u}}_k^2(t) \\ &= \frac{1}{2}\varepsilon^2 + \frac{1}{2}\bar{\bar{\mathbf{u}}}^H(t)(\mathbf{R} - \bar{\lambda}\mathbf{I}_K)\bar{\bar{\mathbf{u}}}(t) + \frac{1}{2}\bar{\lambda} \sum_{k=0}^{K-1} \bar{\bar{u}}_k^2(t) \end{aligned} \tag{31}$$

where $\mathbf{I}_K$ is the identity matrix of order K. Concurrently, $\bar{\bar{u}}_k^2(t) = \bar{E}\{|u_k(t)|^2\}$ is the mean squared value of $u_k(t)$. To solve $\bar{\bar{u}}_k^2(t)$, we can differentiate both sides of the differential equation (9) simultaneously and obtain

$$\begin{aligned} &\frac{d\sum_{k=0}^{L-1} \bar{\bar{u}}_k^2(t)}{dt} + 2(1+\mu\bar{\lambda})\alpha \sum_{k=0}^{L-1} \bar{\bar{u}}_k^2(t) \\ &= 2\alpha Re\{\bar{\bar{\mathbf{u}}}^H(t)\mathbf{h}\} - 2\mu\alpha\bar{\bar{\mathbf{u}}}^H(t)(\mathbf{R} - \bar{\lambda}\mathbf{I}_K)\bar{\bar{\mathbf{u}}}(t). \end{aligned} \tag{32}$$

The solution can be derived as

$$\begin{aligned} \sum_{k=0}^{L-1} \bar{\bar{u}}_k^2(t) &= \mathbf{h}^H \mathbf{Q} diag\left\{ \frac{1}{(1+\mu\lambda_k)^2} + \frac{2\mu\lambda_k}{(1+\mu\lambda_k)^2} e^{-(1+\mu\lambda_k)\alpha t} \right. \\ &\qquad \left. + \frac{(\mu\lambda_k)^2}{(1+\mu\lambda_k)^2} e^{-2(1+\mu\lambda_k)\alpha t} - e^{-2(1+\mu\bar{\lambda})\alpha t} \right\} \mathbf{Q^{-1}h}. \end{aligned} \tag{33}$$

By substituting (30) and (33) into (31), we can obtain the theoretical expression of the residual interference power shown in (22).

Appendix B
Solution for the Inverse Laplace Transform of a k-th Order APF

To find the inverse Laplace transform of $H^{(k)}(s)$, we start with (24) and expand $H^{(k)}(s)$ with the binomial theorem as

$$H^{(k)}(s) = \sum_{k'=0}^{k} \binom{k}{k'} \left(\frac{2\omega_0}{s+\omega_0}\right)^{k'} (-1)^{k-k'}.$$

Then, we consider each term individually. The inverse Laplace transform of $\left(\frac{2\omega_0}{s+\omega_0}\right)^{k'}$ is expressed as

$$\mathcal{L}^{-1}\left\{ \left(\frac{2\omega_0}{s+\omega_0}\right)^{k'} \right\} = \frac{(2\omega_0)^{k'}}{(k'-1)!} t^{k'-1} e^{-\omega_0 t}. \tag{34}$$

By applying the linearity of the inverse Laplace transform to the series expansion, we get

$$\begin{aligned} h^{(k)}(t) &= \mathcal{L}^{-1}\left\{ H^{(k)}(s) \right\} \\ &= \sum_{k'=1}^{k} \binom{k}{k'} (-1)^{k-k'} \frac{(2\omega_0)^{k'}}{(k'-1)!} t^{k'-1} e^{-\omega_0 t}, \quad k > 0. \end{aligned} \tag{35}$$

When $k = 0$, $h^{(0)}(t) = \delta(t)$. Combining these results, the impulse response of k-th APF can be expressed as (25).

REFERENCES

[1] N. C. Luong, X. Lu, D. T. Hoang, D. Niyato, and D. I. Kim, "Radio resource management in joint radar and communication: A comprehensive survey," *IEEE Communications Surveys and Tutorials*, vol. 23, no. 2, pp. 780–814, 2021.

[2] E. Fuchs, T. Handte, D. Verenzuela, and S. T. Brink, "Optimized sequences for nonlinearity estimation and self-interference cancellation," *IEEE Transactions on Communications*, pp. 1–1, 2024.

[3] A. Sabharwal, P. Schniter, D. Guo, D. W. Bliss, S. Rangarajan, and R. Wichman, "In-band full-duplex wireless: Challenges and opportunities," *IEEE Journal on Selected Areas in Communications*, vol. 32, no. 9, pp. 1637–1652, 2014.

[4] K. Komatsu, Y. Miyaji, and H. Uehara, "Basis function selection of frequency-domain hammerstein self-interference canceller for in-band full-duplex wireless communications," *IEEE Transactions on Wireless Communications*, vol. 17, no. 6, pp. 3768–3780, 2018.

[5] Y. He, H. Zhao, and S. Shao, "Nonlinear self-interference cancellation in vehicle networks for full-duplex integrated sensing and communication," *IEEE Transactions on Vehicular Technology*, vol. 73, no. 9, pp. 13 980–13 985, 2024.

[6] Z. H. Hong, L. Zhang, Y. Wu, W. Li, S.-I. Park, S. Ahn, N. Hur, E. Iradier, J. Montalban, and P. Angueira, "Iterative successive nonlinear self-interference cancellation for in-band full-duplex communications," *IEEE Transactions on Broadcasting*, vol. 70, no. 1, pp. 2–13, 2024.

[7] B. Smida, A. Sabharwal, G. Fodor, G. C. Alexandropoulos, H. A. Suraweera, and C.-B. Chae, "Full-duplex wireless for 6G: Progress brings new opportunities and challenges," *IEEE Journal on Selected Areas in Communications*, vol. 41, no. 9, pp. 2729–2750, 2023.

[8] L. Zhang, M. Lv, Z.-Y. Zhang, Y. Wang, F. Zeng, C. Ding, and C. Dai, "A single-antenna full-duplex subsystem with high isolation and high gain," *IEEE Open Journal of Antennas and Propagation*, pp. 1–1, 2024.

[9] H. Zhu, J. Huang, C. Wang, W. Hu, N. Yuan, Q. Wang, C. Zhu, and X. Zhang, "Multi-domain self-interference cancellation methods considering RF imperfections," *IEEE Transactions on Wireless Communications*, pp. 1–1, 2024.

[10] E. Everett, A. Sahai, and A. Sabharwal, "Passive self-interference suppression for full-duplex infrastructure nodes," *IEEE Transactions on Wireless Communications*, vol. 13, no. 2, pp. 680–694, 2014.

[11] Y. N. Chen, C. Ding, H. Zhu, and Y. Liu, "A ±45°-polarized antenna system with four isolated channels for in-band full-duplex," *IEEE Transactions on Antennas and Propagation*, vol. 71, no. 4, pp. 3000–3010, 2023.

[12] H. Li, J. Van Kerrebrouck, O. Caytan, H. Rogier, J. Bauwelinck, P. Demeester, and G. Torfs, "Self-interference cancellation enabling high-throughput short-reach wireless full-duplex communication," *IEEE Transactions on Wireless Communications*, vol. 17, no. 10, pp. 6475–6486, 2018.

[13] M. S. Sim, M. Chung, D. Kim, J. Chung, D. K. Kim, and C.-B. Chae, "Nonlinear self-interference cancellation for full-duplex radios: From link-level and system-level performance perspectives," *IEEE Communications Magazine*, vol. 55, no. 9, pp. 158–167, 2017.

[14] P. Dehghanzadeh, A. Madanayake, H. Zhao, S. B. Venkatakrishnan, and S. Mandal, "A multiport self-interference canceller for wideband simo/mimo-star full-duplex arrays," *IEEE Transactions on Microwave Theory and Techniques*, vol. 72, no. 4, pp. 2640–2654, 2024.

[15] M. N. Anwar Tarek, M. Roman, and E. A. Alwan, "Power efficient rf self-interference cancellation system for simultaneous transmit and receive," in *2021 IEEE International Symposium on Antennas and Propagation and USNC-URSI Radio Science Meeting (APS/URSI)*, 2021, pp. 113–114.

[16] Z. Li, Y. Xia, W. Pei, K. Wang, and D. P. Mandic, "An augmented nonlinear LMS for digital self-interference cancellation in full-duplex direct-conversion transceivers," *IEEE Transactions on Signal Processing*, vol. 66, no. 15, pp. 4065–4078, 2018.

[17] H. Ayar and O. Gurbuz, "Cyclic prefix noise reduction for digital self interference cancellation in ofdm-based in-band full-duplex wireless systems," *IEEE Transactions on Wireless Communications*, vol. 20, no. 9, pp. 6224–6238, 2021.

[18] K. E. Kolodziej, A. U. Cookson, and B. T. Perry, "Adaptive learning rate tuning algorithm for rf self-interference cancellation," *IEEE Transactions on Microwave Theory and Techniques*, vol. 69, no. 3, pp. 1740–1751, 2021.

[19] S.-M. Kim, Y.-G. Lim, L. Dai, and C.-B. Chae, "Performance analysis of self-interference cancellation in full-duplex massive mimo systems: Subtraction versus spatial suppression," *IEEE Transactions on Wireless Communications*, vol. 22, no. 1, pp. 642–657, 2023.

[20] A. T. Le, X. Huang, C. Ding, H. Zhang, and Y. J. Guo, "An in-band full-duplex prototype with joint self-interference cancellation in antenna, analog, and digital domains," *IEEE Transactions on Microwave Theory and Techniques*, pp. 1–10, 2024.

[21] J. W. Kwak, M. S. Sim, I.-W. Kang, J. Park, K.-K. Wong, and C.-B. Chae, "Analog self-interference cancellation with practical RF components for full-duplex radios," *IEEE Transactions on Wireless Communications*, vol. 22, no. 7, pp. 4552–4564, 2023.

[22] S.-A. Ayati, A. Alizadeh, and S. Kiaei, "Cmos full-duplex mixer-first receiver with adaptive self-interference cancellation," *IEEE Transactions on Circuits and Systems I: Regular Papers*, vol. 68, no. 2, pp. 868–878, 2021.

[23] X. Huang and Y. J. Guo, "Radio frequency self-interference cancellation with analog least mean-square loop," *IEEE Transactions on Microwave Theory and Techniques*, vol. 65, no. 9, pp. 3336–3350, 2017.

[24] Y. Liu, P. Roblin, X. Quan, W. Pan, S. Shao, and Y. Tang, "A full-duplex transceiver with two-stage analog cancellations for multipath self-interference," *IEEE Transactions on Microwave Theory and Techniques*, vol. 65, no. 12, pp. 5263–5273, 2017.

[25] T. Fukui, K. Komatsu, Y. Miyaji, and H. Uehara, "Analog self-interference cancellation using auxiliary transmitter considering iq imbalance and amplifier nonlinearity," *IEEE Transactions on Wireless Communications*, vol. 19, no. 11, pp. 7439–7452, 2020.

[26] J. W. Kwak, M. S. Sim, I.-W. Kang, J. S. Park, J. Park, and C.-B. Chae, "A comparative study of analog/digital self-interference cancellation for full duplex radios," in *2019 53rd Asilomar Conference on Signals, Systems, and Computers*. IEEE, 2019, pp. 1114–1119.

[27] B. King, J. Xia, and S. Boumaiza, "Digitally assisted RF-analog self interference cancellation for wideband full-duplex radios," *IEEE Transactions on Circuits and Systems II: Express Briefs*, vol. 65, no. 3, pp. 336–340, 2018.

[28] H. Luo, M. Holm, and T. Ratnarajah, "Wideband active analog self-interference cancellation for 5G and beyond full-duplex systems," in *2020 54th Asilomar Conference on Signals, Systems, and Computers*, 2020, pp. 868–872.

[29] C. W. Morgenstern, Y. Rong, A. Herschfelt, A. C. Molnar, A. B. Apsel, D. G. Landon, and D. W. Bliss, "Analog-domain self-interference cancellation for practical multi-tap full-duplex system: Theory, modeling, and algorithm," *IEEE Journal on Selected Areas in Communications*, vol. 41, no. 9, pp. 2796–2807, 2023.

[30] T. Zhang, C. Su, A. Najafi, and J. C. Rudell, "Wideband dual-injection path self-interference cancellation architecture for full-duplex transceivers," *IEEE Journal of Solid-State Circuits*, vol. 53, no. 6, pp. 1563–1576, 2018.

[31] L. Zhang, M. Ma, and B. Jiao, "Design and implementation of adaptive multi-tap analog interference canceller," *IEEE Transactions on Wireless Communications*, vol. 18, no. 3, pp. 1698–1706, 2019.

[32] A. Herschfelt, A. Chiriyath, A. C. Molnar, D. G. Landon, and D. W. Bliss, "In-band, full-duplex self-interference mitigation using sparse tap-delay models with quantized and power constrained weights," in *2020 54th Asilomar Conference on Signals, Systems, and Computers*, 2020, pp. 1260–1264.

[33] H. Qin, J. Meng, F. He, Q. Wang, and B. Li, "Design and analysis of digital-to-analog hybrid RF interference cancellation system based on multitap structure," *IEEE Transactions on Microwave Theory and Techniques*, vol. 69, no. 9, pp. 4300–4314, 2021.

[34] D. H. Kong, Y.-S. Kil, and S.-H. Kim, "Neural network aided digital self-interference cancellation for full-duplex communication over time-varying channels," *IEEE Transactions on Vehicular Technology*, vol. 71, no. 6, pp. 6201–6213, 2022.

[35] T. Kebede, Y. Wondie, J. Steinbrunn, H. B. Kassa, and K. T. Kornegay, "Multi-carrier waveforms and multiple access strategies in wireless networks: Performance, applications, and challenges," *IEEE Access*, vol. 10, pp. 21 120–21 140, 2022.

[36] K. E. Kolodziej, J. G. McMichael, and B. T. Perry, "Multitap RF canceller for in-band full-duplex wireless communications," *IEEE Transactions on Wireless Communications*, vol. 15, no. 6, pp. 4321–4334, 2016.

[37] K. E. Kolodziej, S. Yegnanarayanan, and B. T. Perry, "Fiber bragg grating delay lines for wideband self-interference cancellation," *IEEE Transactions on Microwave Theory and Techniques*, vol. 67, no. 10, pp. 4005–4014, 2019.

[38] X. Huang, H. Zhang, A. T. Le, J. A. Zhang, and Y. J. Guo, "Digital post-cancellation of nonlinear interference for millimeter wave and terahertz systems," *IEEE Transactions on Wireless Communications*, pp. 1–1, 2024.